



Fabrication of BiOIO₃ with induced oxygen vacancies for efficient separation of the electron-hole pairs

Xiaoming Sun^a, Jiang Wu^{a,*}, Qifan Li^a, Qizhen Liu^b, Yongfeng Qi^c, Ling You^c, Zheng Ji^a, Ping He^a, Pengfei Sheng^a, Jianxing Ren^a, Wenbo Zhang^a, Jia Lu^a, Jinjing Zhang^a

^a College of Energy and Mechanical Engineering, Shanghai University of Electric Power, Shanghai 200090, China

^b Shanghai Environment Monitoring Center, Shanghai 200030, China

^c School of Hydraulic Energy and Power Engineering, Yangzhou University, Yangzhou 225002, China

ARTICLE INFO

Article history:

Received 31 January 2017

Received in revised form 27 April 2017

Accepted 15 June 2017

Available online 16 June 2017

Keywords:

BiOIO₃

Calcination method

Oxygen vacancy

Mercury

ABSTRACT

Bismuth-based nanomaterials exhibiting unique structures, which endow them with fascinating physicochemical properties, have received more and more interests as promising photocatalysts. Fabrication of BiOIO₃ photocatalysts by calcination method was investigated for the first time. XRD patterns showed that the crystallinity of BiOIO₃ photocatalysts could be controlled by calcination temperature. TGA demonstrated that calcining the precursor at a specific temperature range was appropriate for preparing BiOIO₃ photocatalysts. XPS and FT-IR characterization revealed that the BiOIO₃ photocatalysts prepared by calcination method possessed oxygen vacancies, which acted as the positive charge centers to trap the electron easily, inhibiting the recombination of photo electron-hole pairs. Furthermore, PL spectra confirmed the oxygen vacancies can favor for the separation of the electron-hole pairs and in turn enhance the photocatalytic performance. From the above analysis, the mechanism of preparing BiOIO₃ photocatalysts by calcination method was proposed. Meanwhile, the effect of oxygen vacancies on the photocatalytic activity of BiOIO₃ photocatalysts was investigated. The BiOIO₃ photocatalysts with oxygen vacancies were found to be efficiently photocatalytically remove gaseous Hg⁰ and the relative photocatalysis mechanism was investigated.

© 2017 Published by Elsevier B.V.

1. Introduction

Mercury is of high toxicity, volatility and persistent bioaccumulation in the environment, and anthropogenic activities play a dominated role in the mercury and its derivatives emission [1], of which the mercury emission in the flue gas at coal combustion power stations holds about one quarter. The US Environment Protection Agency (EPA) issued the national standard of Final Mercury and Air Toxics Standards for the control of mercury in 2012 [2]. The Minamata Convention resulted in signed agreements to regulate Hg⁰ emissions in 2013. The Ministry of Environmental Protection of China established new emission standard of mercury for power plants and restricted mercury emission in 0.03 mg/m³ after 2015 [3]. Therefore, improving the removal efficiency of mercury from power plant has become an urgent issue. There exist three forms of mercury in the coal-fired power plant: elemental mercury(Hg⁰), particulate-bound mercury(Hg^P), and oxidized mercury(Hg²⁺) [4,5]. The oxidized mercury(Hg²⁺) can be removed

by wet flue-gas desulfurization (WFGD) [6,7]. Particulate-bound mercury(Hg^P) can be captured by fabric filter(FF) or an electrostatic precipitator(ESP) [8,9]. However, it is difficult to remove elemental mercury due to its high volatility and slight solubility [10,11].

There are various methods for elemental mercury emission control, such as using the existing air pollutant control devices (APCDs) at power stations, chemical injection in the duct, and some new methods. Activated carbon injection is a mature method for elemental mercury removal [12], but its high operation cost and negative effects on fly ash quality may restrict its industrial application. Recently, many researchers have confirmed photocatalysis is a promising process to remove gas-phase mercury because of low energy consumption and non-secondary-pollution [13–15]. However, low rate of electron transfer and fast combination of electron-hole pairs seriously limited the reaction of photocatalysis. Therefore, it is very necessary to control recombination of the photoinduced electron-hole pairs to enhance the photocatalytic performance of photocatalysts.

A surface oxygen vacancy, an intrinsic defect on the surface of photocatalysts, has a remarkable effect on the electronic structure and physical-chemical properties of photocatalysts, which is favorable for the separation of the electron-hole pairs [16,17]. The

* Corresponding author at: NO. 2103 Pingliang Road, Shanghai 200090, China.

E-mail address: wjcfd2002@sina.com (J. Wu).

oxygen vacancies can be the centers for capturing photoinduced electrons in the photocatalytic reaction since the photoinduced electrons in the conduction band(CB) are preferentially transferring to oxygen vacancies rather than photoinduced holes. Hence, developing the photocatalysts with the oxygen vacancies is important for efficient separation of electron-hole pairs and in turn to enhance the photocatalytic performance.

In recent years, bismuth-based layered nanomaterials have received more and more interests as promising photocatalysts because their unique structures endow them with fascinating physicochemical properties [18,19]. BiOIO₃ is one of bismuth-based layered nanomaterials containing two long pair cations, Bi³⁺ and I⁵⁺, exhibiting an Aurivillius-type (Bi₂O₂)²⁺ layer. Many groups researched the BiOIO₃ nanomaterials' photocatalytic performance from different perspectives. Sau et al. synthesized BiOIO₃ by hydrothermal method and its crystal structure, polarization, and electronic structure were analyzed in detail [20]. Wang et al. synthesized BiOIO₃ nanoplates by hydrothermal method and put forward that the enhanced photocatalytic properties of BiOIO₃ nanoplates were attributed to heterolayered structure and internal polar field [21]. Qi et al. prepared BiOIO₃ photocatalysts at different pH via a facial hydrothermal method and found the morphology and crystal structure of BiOIO₃ products could be controlled by pH of precursors [22]. Meanwhile, many researchers fabricated BiOI/BiOIO₃ [23–25], BiOBr/BiOIO₃ [26], AgI/BiOIO₃ [27], carbon spheres-BiOI/BiOIO₃ [28], RGO/BiOIO₃ [29], C₃N₄/BiOIO₃ [30] and I⁻ doping BiOIO₃ [31] to enhance the BiOIO₃ nanomaterials' photocatalytic performance. However, to the best of our knowledge, fabrication of BiOIO₃ photocatalysts with oxygen vacancies has seldom been reported. It is rational to assume that fabrication of BiOIO₃ photocatalysts by a regular method, i.e., hydrothermal method, is difficult to induce oxygen vacancies.

Many research groups confirmed that calcination method can efficiently induce oxygen vacancies and the optimum preparation condition can be attained by controlling the calcination temperature. Pan et al. synthesized defective TiO₂ with oxygen vacancies by calcination method and proposed that the oxygen vacancies endowed the defective TiO₂ with unique physical and chemical properties in favor of visible light absorption, dissociative adsorption and reductive properties [32]. Wang et al. synthesized ZnO photocatalysts by calcination method and found the oxygen vacancies could induce band-gap narrowing [33]. Wang et al. synthesized N-doped TiO₂ by calcination method and found the highest photocatalytic performance was attributed to the formation of single-electron-trapped oxygen vacancy [34].

In this paper, we applied calcination method for fabricating BiOIO₃ nanomaterials, and found the calcination method could induce oxygen vacancies on the surface of BiOIO₃ photocatalysts. The existence of surface oxygen vacancies was substantially confirmed by X-ray photoelectron spectroscopy (XPS) and in situ Fourier transform infrared (FT-IR). Furthermore, Photoluminescence spectra (PL) confirmed the oxygen vacancies can favor for the separation of the electron-hole pairs and in turn enhance photocatalytic performance. The as-prepared bismuth-based semiconductors prepared by calcination method and hydrothermal method, which was as the comparison, were applied to photocatalytic removal on gaseous Hg⁰⁰ under LED light irradiation, and the relative photocatalysis mechanism was investigated.

2. Experimental

2.1. Chemicals and materials

Bismuth nitrate pentahydrate(Bi(NO₃)₃·5H₂O) and potassium iodate(KIO₃) were both obtained from Guoyao Chemical Reagent

Co. Ltd. All solutions were prepared with deionized water and all chemicals used were analytical grade and were used without further purification.

2.2. Preparation of BiOIO₃ nanomaterials

BiOIO₃ photocatalysts with oxygen vacancies were prepared through a simple calcination procedure. In a typical reaction, bismuth nitrate pentahydrate (0.485 g, 1 mmol) was added to deionized water (80 ml) under constant stirring 10 min, and then potassium iodate (0.214 g, 1 mmol) was dissolved in the above suspension. After stirring for 2 h in dark, the product was obtained by filtering and was washed with deionized water and absolute ethyl alcohol for three times and then dried at 80 °C for 12 h. The obtained product was ground into powders, then calcined in the muffle furnace for 2 h (the rate of heating was set as 2 °C/min) under different temperatures (100 °C, 200 °C, 300 °C, 400 °C, 500 °C, 600 °C, 700 °C). In the end, a series of samples were ground into powders. We denoted the samples prepared at 100 °C, 200 °C, 300 °C, 400 °C, 500 °C, 600 °C and 700 °C as C-100, C-200, C-300, C-400, C-500, C-600 and C-700 respectively. The sample which was not calcined in the muffle furnace denoted as C-0.

As comparison pairs, BiOIO₃ photocatalysts were also prepared through a simple hydrothermal procedure reported in our previous work [25]. In a typical reaction, bismuth nitrate pentahydrate (0.485 g, 1 mmol) was added to deionized water (80 ml) under constant stirring for 10 min, and then potassium iodate (0.214 g, 1 mmol) was dissolved in the above suspension. After stirring for 30 min, the mixture was transferred into a 100 ml Teflonlined stainless autoclave. The autoclave was sealed and heated at 150 °C for 5 h. After naturally cooling down to room temperature, the product was obtained by filtering and was washed with deionized water and absolute ethyl alcohol three times and then dried at 80 °C for 12 h. We denoted the BiOIO₃ nanomaterials prepared through a hydrothermal procedure as H-150.

2.3. BiOIO₃ nanomaterials characterization

X-ray diffractometer (XRD) were taken on a BRUKER D8 ADVANCE Diffractometer. XRD data were collected from 20 = 20–80° (step 0.01°, scan rate 2°min⁻¹) using Cu K α X-rays (λ =1.5418 Å, 40 mA, 40 kV). Thermo-gravimetric analysis (TGA) were performed on a NETZSCH STA 409 PC/PG thermogravimetric analyzer. C-0 precursor was heated in air from room temperature (20 °C) to 800 °C at heating rate of 10 °C/min. XPS with Al K α X-ray ($h\nu$ =1486.6 eV) radiation operated at 250 W (PHI5300, USA) was used to investigate the surface properties. The morphology of the catalyst was determined using a scanning electron microscope (SEM, Phillips XL-30 FEG/NEW). Transmission electron microscopy (TEM) and high-resolution transmission electron microscopy (HRTEM) image were used to further analyze the morphology and crystallinity of the products on a Phillips Model CM200 transmission electron microscope. UV-vis absorbance spector were recorded over the range 250–800 nm on a UV-vis spectrophotometer (SHIMADZU UV-3600, Japan). Barium sulfate (BaSO₄) was used as a reference standard. PL were performed in air at room temperature using a fluorescence spectrophotometer (Edinburgh FLS920 phosphorimeter). Spectra were excited at 310 nm and photoluminescence spectra were recorded over a range of 350–550 nm using a standard photomultiplier.

2.4. Measurement of photoactivity

The photocatalytic activity was evaluated using a laboratory scale test system, which was similar to that used in our previous study [35] and was shown in Fig. 1. The system was consisted of

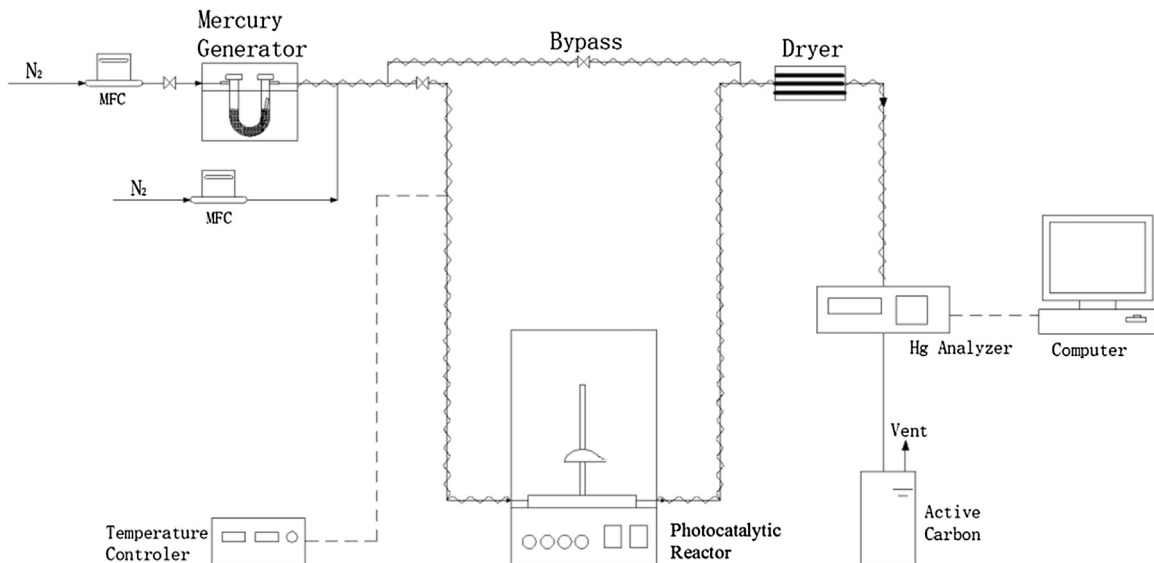
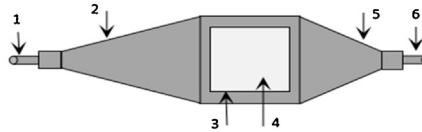


Fig. 1. Schematic diagram of the experimental system. 1. N_2 inlet 2. inlet transition zone 3. quartz glass cover Plate 4. reaction zone 5. outlet transition zone 6. N_2 outlet.



1. N_2 inlet 2. inlet transition zone 3. quartz glass cover plate 4. reaction zone 5. outlet transition zone 6. N_2 outlet.

Fig. 2. Schematic of the photocatalytic reactor.

simulated flue gas system, a photocatalytic reactor and a mercury analyzer. The N_2 was divided into two branches, and each flow rate was controlled by a mass flow meter (MFC, CS200 type). The total flow of the two branches was 1.2L/min. One gas stream with a flow rate of 0.2L/min passed through the Hg^0 permeation tube to introduce Hg^0 vapor into the system. The mercury permeation tube was placed in a U-shape glass tube which was immersed in a constant 50 °C water bath to ensure a constant Hg^0 permeation rate. The Hg^0 inlet concentration was around 60 $\mu\text{g}/\text{m}^3$, the atmospheric air humidity was approximately 0.6% and the atmospheric temperature was approximately 15 °C. The other stream of N_2 was with a flow rate of 1L/min. Two shares of gas mixed in the mixing tank. The gas out of the mixing tank through adjustment of the three-way valve and the two-way valve respectively into the photocatalytic reactor and the bypass, and the gas after reaction or the gas of bypass passed silica gel into the LUMEX type of gas-line mercury analyzer to measure the gas phase concentration of Hg^0 . Finally, the gas got through the exhausted gas absorption bottle and was emitted.

The Hg^0 test was carried out with the as-prepared photocatalysts loaded on the quartz glass under an 18W LED light irradiation, whose wavelength was approximately 400–450 nm. The as-prepared sample was dissolved in 5 ml alcohol, then shocked with ultrasonic for 10 min. After that, the glass fabric attached with a photocatalyst was dried in an oven at around 80 °C for 10 min. The above process was repeated three times so that sufficient photocatalyst was loaded on the quartz glass, then it was put into the photocatalytic reactor developed by ourselves, which was shown in Fig. 2. The photocatalytic reactor was consisted of inlet transition zone, reaction zone and outlet transition zone. The loaded photo-

catalyst was about 50 mg. In order to describe this phenomenon in detail, the Hg^0 removal efficiency was defined as following:

$$\eta_{Hg} = \frac{Hg_{inlet}^0 - Hg_{outlet}^0}{Hg_{inlet}^0} \times 100\%$$

The Hg_{inlet}^0 represented Hg^0 at the inlet of reactor, and Hg_{outlet}^0 represented Hg^0 at the outlet of the reactor.

3. Results and discussions

3.1. $BiOIO_3$ photocatalysts characterization

3.1.1. XRD analysis

The XRD patterns of the as-prepared $BiOIO_3$ photocatalysts through the calcination method were shown in Fig. 3. C-100 was bismuth oxide nitrate hydrate illustrated in Fig. 3, which was in accordance with Crystal Structure Database (CSD #8077), meaning that C-100 nanomaterial contained some surface chemisorbed water and residual nitrate. When being calcined at the temperature range from 200 °C to 400 °C, C-200, C-300 and C-400 were all $BiOIO_3$ photocatalysts. Furthermore, the crystallinity of $BiOIO_3$ photocatalysts could be adjusted by changing calcination temperature. The C-500 was in good accordance with the orthorhombic Bi_5O_7I (PDF #40-0548), meaning that $BiOIO_3$ was transformed into Bi_5O_7I when the calcination temperature increased from 400 °C to 500 °C. C-600 was well consistent with the orthorhombic Bi_5O_7I , meaning that Bi_5O_7I was successfully synthesized when $BiOIO_3$ was calcined at temperature range from 500 °C to 600 °C [30]. When the calcination temperature increased

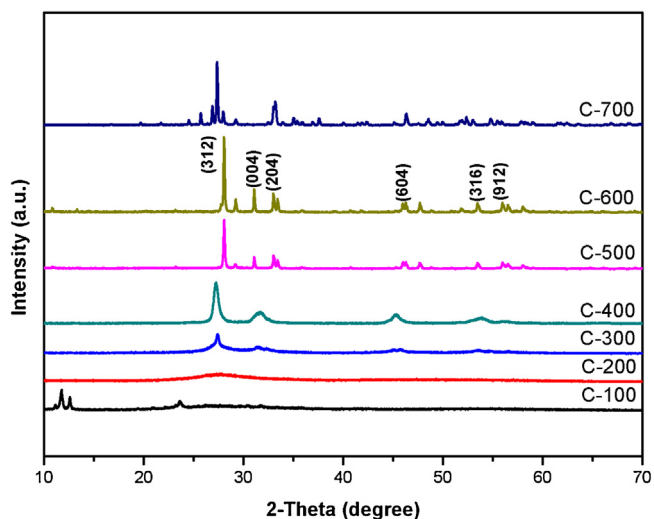


Fig. 3. XRD patterns of C-100, C-200, C-300, C-400, C-500, C-600, and C-700.

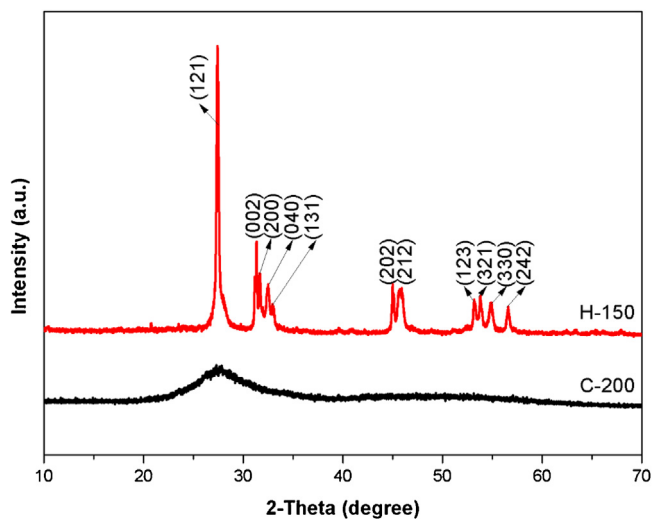


Fig. 4. XRD patterns of H-150 and C-200.

to 700 °C, Bi₅O₇I degraded to Bi₂O₃, i.e., C-700, whose XRD pattern shown in Fig. 3 was in accordance with Crystal Structure Database (CSD #2374).

Fig. 4 showed the comparison of XRD characterization between H-150 and C-200. H-150 was indexed as orthorhombic BiOIO₃ (space group: pca21; $a=5.6584(4)$, $b=11.0386(8)$, $c=5.7476(4)$). The intense and sharp diffraction peaks of H-150 demonstrated that the synthesized nanomaterial was well crystallized and was in good accordance with the Inorganic Crystal Structure Database (ICSD #262019). The (121) plane was extremely strong, indicating that the preferential growth of H-150 was along the (121) direction. The XRD pattern of C-200 had no obvious

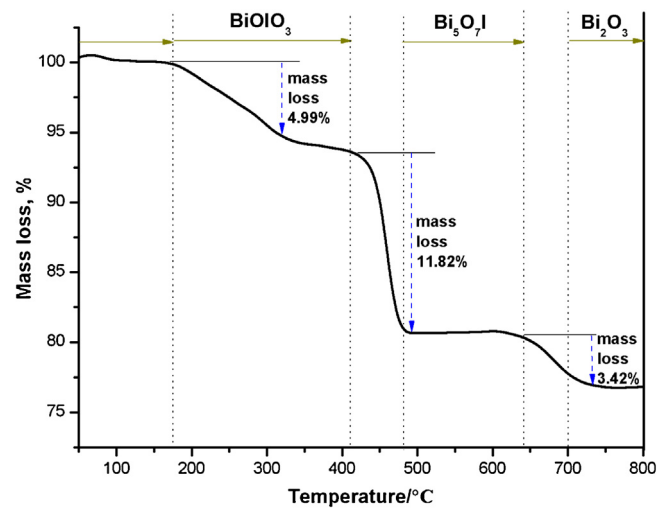


Fig. 5. TGA curves of C-0.

diffraction peak, which revealed that calcination at 200 °C for 2 h could synthesize low crystalline BiOIO₃ photocatalysts. In a word, we successfully synthesized pure BiOIO₃ nanomaterials through hydrothermal and calcination method respectively, both of which were in good accordance with XRD patterns.

3.1.2. TGA characterization

Thermogravimetric analysis is an efficient way for studying the mass loss of the as-prepared samples under the heating process. TGA curve for the C-0 heating in air from 20 °C to 800 °C was shown as Fig. 5 and Fig. 6. C-0 was a nanomaterial precursor before being calcined in a muffle furnace. Fig. 5 showed that when heating temperature changed from 20 °C to 200 °C, there was tiny mass loss, because the nanomaterial was dried in an oven at 80 °C for 12 h before TGA characterization. When the heating temperature changed from 200 °C to 300 °C, the mass loss was 5% due to thermal desorption of surface chemisorbed water and residual nitrate after thermal volatilization. There was no obvious mass change during heating from 300 °C to 400 °C, meaning that BiOIO₃ had a stability up to 400 °C [20]. Between 400 °C to 500 °C, there was a sharp mass loss due to BiOIO₃ transferring into Bi₅O₇I and the result agreed well with XRD analysis shown in Fig. 3. There was a 3.42% mass loss when being heated from 700 °C to 800 °C, which means Bi₅O₇I nanomaterials were degraded to Bi₂O₃ slowly. TGA characterization indicated that the C-0 precursor calcined at a temperature ranging from 200 °C to 400 °C for 2 h was appropriate for preparing BiOIO₃ photocatalysts, and the C-0 precursor calcined at a temperature ranging from 500 °C to 600 °C for 2 h was appropriate for preparing Bi₅O₇I photocatalysts.

3.1.3. XPS analysis

The surface chemical composition and chemical states of BiOIO₃ photocatalysts fabricated by hydrothermal method and calcination method were analyzed by XPS. In Fig. 7, the XPS survey spectra of H-

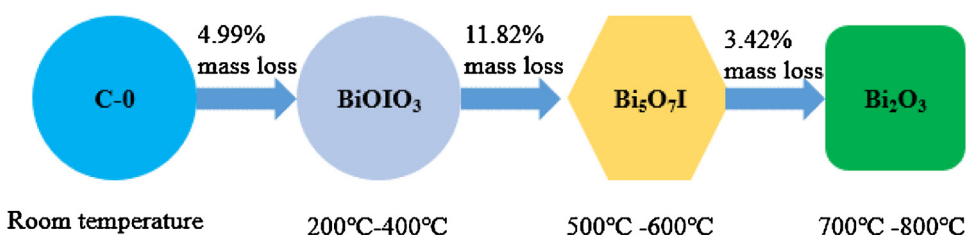


Fig. 6. Synthesis process of BiOIO₃ and Bi₅O₇I photocatalysts.

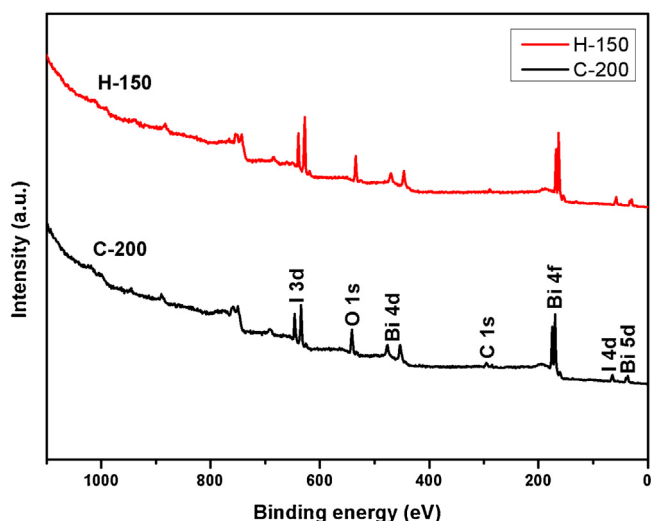


Fig. 7. XPS spectrum of H-150 and C-200.

150 and C-200 suggested that the BiOIO_3 photocatalysts contained C, Bi, O and I, which was consistent with chemical composition of the as-prepared photocatalysts. The tiny C 1 s peak at around 284.6 eV could be assigned to the adventitious carbon depositing on the surface of photocatalysts and was used for calibration [36]. Bi 4f, O 1s and I 3d X-ray photoelectron spectroscopy (XPS) results of the H-150 and C-200 samples were shown in Fig. 8. Based on the high resolution Bi 4f spectrum of H-150 (Fig. 8a.), the peaks at 158.90 and 164.00 eV could be ascribed to levels of Bi $4f_{5/2}$ and Bi $4f_{7/2}$ spin-orbital splitting photoelectrons in the Bi^{3+} chemical state respectively [21,31]. Compared to H-150, the Bi 4f photoelectron peaks of C-200 samples shifted to higher binding energy with the formation of surface bismuth defects [37,38]. Three peaks with binding energies of 529.35, 530.46 and 531.86 eV were observed in the high-resolution O 1s spectra of H-150 (Fig. 8b.). The primary peak at 529.35 eV was attributed to the lattice oxygen O^{2-} (in the stronger Bi-O band) [39,40], the secondary one at 530.46 eV was assigned to the I-O band in BiOIO_3 [41], and the third one at a higher bonding energy of 531.86 eV was ascribed to the surface absorbed oxygen(-OH group and chemisorbed oxygen-containing species)[42,43]. These peaks in C-200 shifted to 529.33, 530.45 and 532.31 eV. It is believed that the intensity of this peak was connected to the variations in the concentration of oxygen vacancies[44]. Therefore, changes in the intensity of the concentration of this component may be connected in part to the variations in the concentration of oxygen vacancies. By comparing the O 1s spectra of H-150 (Fig. 8b) and C-200 (Fig. 8d), we can find that the third one at 532.31 eV was obviously stronger in C-200 samples than that in H-150 samples, which confirmed the BiOIO_3 fabricated by calcination method had a higher concentration of oxygen vacancies. The I 3d XPS spectra of H-150 in Fig. 8c could be observed at binding energies of 623.60(I 3d_{3/2}) and 635.20eV(I 3d_{5/2}) corresponding to I⁵⁺ in BiOIO_3 . A positive shift in the I⁵⁺ binding energies was also observed in the C-200 samples. These results also implied that there were high concentration of oxygen vacancies in the C-200 samples.

3.1.4. SEM analysis

The FESEM images of BiOIO_3 photocatalysts prepared by calcination method at a temperature range from 200 °C to 400 °C and prepared by hydrothermal method were shown in Fig. 9. C-200 had porous structure and contained some nanoplate particles. When temperature was up to 300 °C, the porous structure collapsed and the nanoplates developed to nanosheets, which meant C-300 was with similar morphology to that of H-150. When being

Table 1
Summarized N_2 physisorption data for the C-200, C-300, C-400, and H-150.

Sample	BET surface area (m^2g^{-1})	Pore volume (cm^3g^{-1})	Pore diameter (nm)
C-200	10.18	0.0611	24.0069
C-300	8.61	0.0482	22.4309
C-400	7.57	0.0293	15.4765
H-150	18.02	0.1161	25.7925

heated to 400 °C, the nanosheets changed into flocculent structure. The BiOIO_3 nanomaterial synthesized via hydrothermal method(H-150) had a nanosheet morphology. The edge was about 120 nm in length and 60 nm in width, which was similar to our previous report. Consequently, C-200 heated in muffle furnace at 200 °C for 2 h was the best condition to fabricate BiOIO_3 nanomaterials.

3.1.5. TEM analysis

Fig. 10(a) and (b) showed the images of C-200 calcined at 200 °C for 2 h. Shown as Fig. 10(a), the crystallinity of C-200 was so low that it could not identify the crystal lattice, which was in accordance with XRD patterns. Fig. 10(b) demonstrated that the BiOIO_3 nanomaterials fabricated via calcination method possessed small size with the diameter of about 20 ~ 30 nm. The C-200 nanomaterials overlapped together, meaning that the BiOIO_3 nanomaterials fabricated by calcination method were scattered unevenly. From Fig. 10(c), it can be seen that H-150 was with lattice fringes and the spacing was 0.323 nm, agreeing well with the spacing of the (121) plane of BiOIO_3 . Fig. 10(d) described that the diameter of the BiOIO_3 nanomaterials fabricated through hydrothermal method was about 100 ~ 120 nm, being in good agreement with the SEM analysis. To sum up, the sizes of BiOIO_3 nanomaterials fabricated by calcination method were smaller than the sizes of BiOIO_3 nanomaterials fabricated by hydrothermal method, which was confirmed by both SEM and TEM analysis.

3.1.6. BET analysis

As illustrated in Table 1 and Fig. 11, the N_2 adsorption-desorption isotherm curves of BiOIO_3 photocatalysts fabricated by hydrothermal and calcination method are both type IV based on IUPAC categorization. The hysteresis loop extends from $P/P_0 = 0.05$ to $P/P_0 = 1$, so it proves that the as-prepared BiOIO_3 photocatalysts by both of hydrothermal and calcination method were mesoporous and microporous materials. The C-200, C-300 and C-400 featured mesoporous structures, which could be confirmed by SEM characterization. The H-150 had a stacking of nanosheets morphology, which was the main factor of forming porous structure, being in good accordance with our previous reports[25,28].

3.1.7. FT-IR analysis

Fig. 12 showed FT-IR adsorption spectrum of C-200, C-300, C-400 and H-150 samples. FT-IR is an effective way to characterize the local structure and constituent of samples, providing some useful information relevant to the bonding states of the compounds. In Fig. 12, the bending vibrations (3435 cm^{-1}) corresponding to the O-H vibration include hydroxyl groups and tiny physically absorbed water. In the photocatalytic process, the hydroxyl groups and tiny physically absorbed water can be trapped by holes under LED light irradiation and then generate hydroxyl radicals, which can enhance the photocatalytic efficiency. The bending vibrations at 1390 cm^{-1} was potassium nitrate, which is corresponding to potassium nitrate attained from the reaction between the precursors, i.e., bismuth nitrate pentahydrate and potassium iodate. The XRD and TGA analysis indicated that the C-O was bismuth oxide nitrate hydroxide hydrate, which was transferred into the nucleus BiOIO_3 after being calcined at 200 °C for 2 h, however there was a lit-

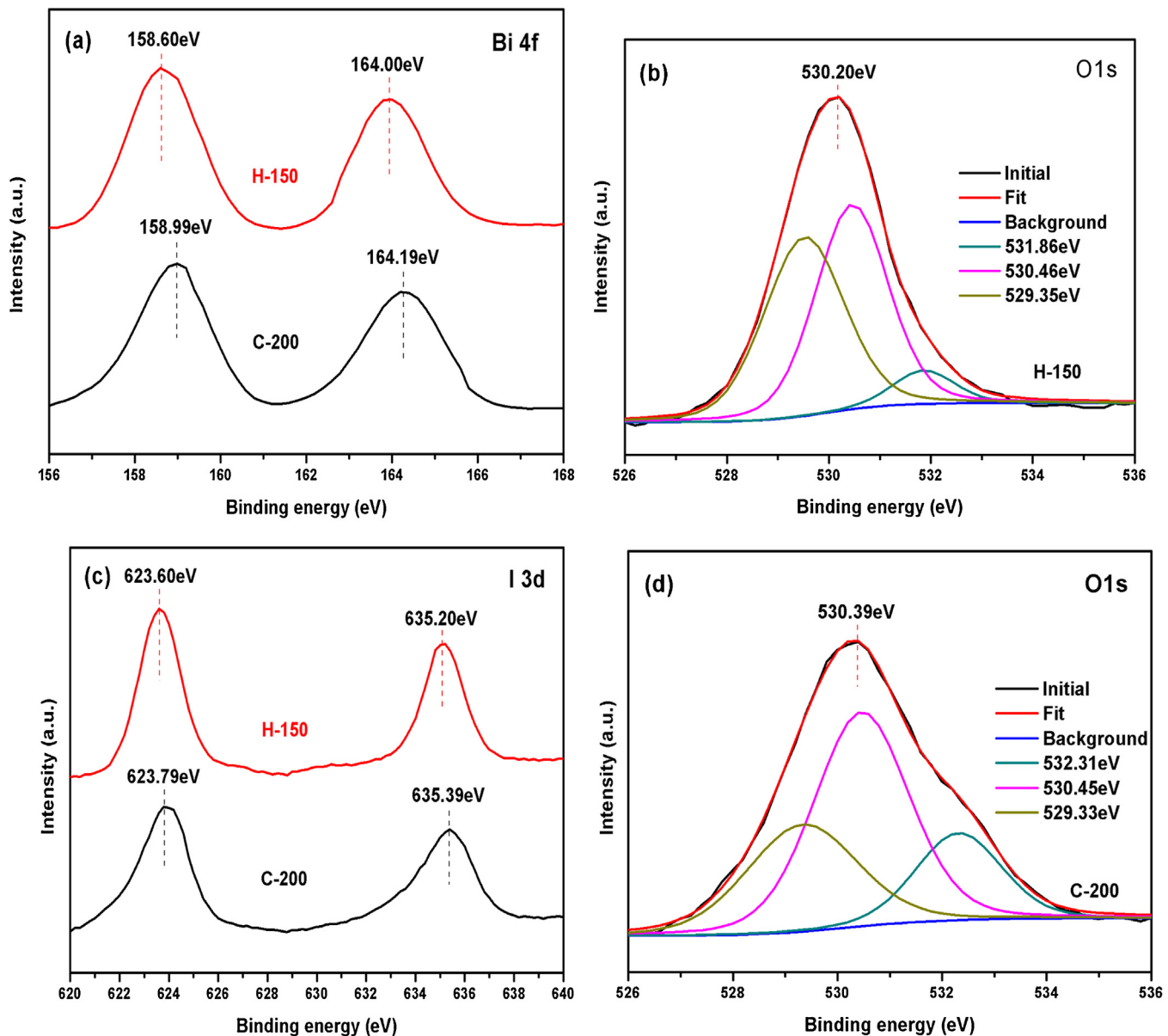


Fig. 8. Bi 4f(a), O 1s(b, d) and I 3d(c) XPS spectrum of H-150 and C-200.

tle potassium nitrate remaining in the catalysts. The strong bands at about 773 cm^{-1} and 687 cm^{-1} were assigned to I-O stretching vibration.

Generally, the band at about 516 cm^{-1} was assigned to the vibration of Bi-O band. However, interestingly, the Bi-O band of C-200 had a red-shift from 516 cm^{-1} to 541 cm^{-1} . According to the classic vibration theory, with the increasing of oxygen vacancies, the interface and space charges, which can provide a force to block movement of electric dipoles and ferroelectric domains, decreases. Oxygen vacancies were introduced into the C-200[38], making the interface and space charges in C-200 decrease, which led the increase of dielectric constant, so electric dipoles can move and rotate more freely[45,46], thus the red shift from 516 cm^{-1} to 541 cm^{-1} was identified in the FT-IR spectra. Meanwhile, the I-O band of C-400 had a mild red shift, which can be attributed to the tiny BiOIO_3 degradation to $\text{Bi}_5\text{O}_7\text{I}$.

3.1.8. UV-vis DRS analysis

The optical properties of BiOIO_3 nanomaterials through calcination method at different temperatures were confirmed by

UV-vis diffuse reflectance spectroscopy in Fig. 13. The visible light absorption spectra differed considerably depending on calcination temperature. C-200 had a 400 nm absorption edge. When calcination temperature was up to $300\text{ }^\circ\text{C}$, C-300 had a 410 nm absorption edge. C-400 displayed intense absorption of light with wavelength below 430 nm because it contained a few $\text{Bi}_5\text{O}_7\text{I}$ composites.

Fig. 14 showed the optical properties of BiOIO_3 nanomaterial prepared via hydrothermal and calcination methods. For a semiconductor, the band gap energy is described by the following equation: $\alpha h\nu = A(h\nu - E_g)^n$, where α is the absorption coefficient, $h\nu$ is the photon energy, A is a constant and E_g is the energy band gap. BiOIO_3 is an indirect transition semiconductor, so $n=2$. From the $(\alpha h\nu)^{1/2}$ vs $h\nu$ plot (Fig. 14), the band gap energy of C-200 and H-150 are about 3.10 eV and 3.02 eV respectively. The valence band-edge potential of a semiconductor can be calculated by the empirical equation $E_{VB} = \chi - E^e + 0.5E_g - 0.5E_g$, where χ is the electronegativity of the semiconductor atoms, E^e is the energy of free electrons on the hydrogen scale (about 4.5 eV), E_g is the band gap energy of a semiconductor. The CB bottom, E_{CB} , can be determined by $E_{CB} = E_{VB} - E_g$. The χ value of BiOIO_3 is about 7.04 eV, so the E_{VB} of C-200 and H-

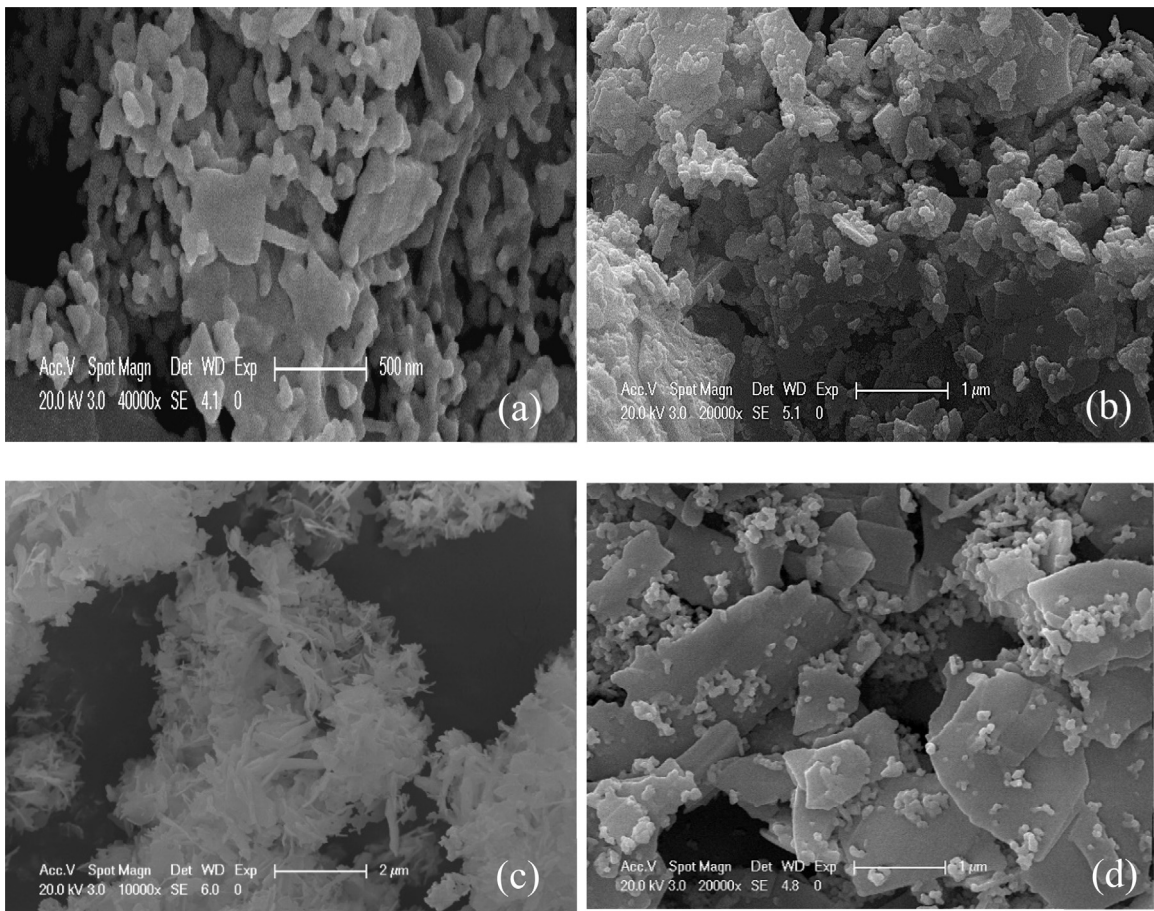


Fig. 9. SEM images of C-200(a), C-300(b), C-400(c), H-150(d).

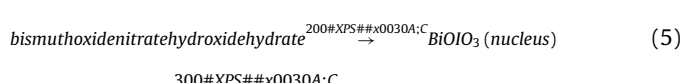
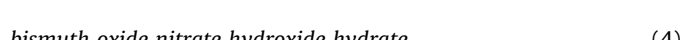
150 are calculated to be 4.09 eV and 4.05 eV, and the E_{CB} of C-200 and H-150 is calculated to be 0.99 eV and 1.03 eV respectively.

3.1.9. Photoluminescence spectra

For deep insight into how oxygen vacancies affect the photocatalytic activity of BiOIO_3 photocatalysts, we conducted the photoluminescence(PL) measurements. The photogenerated electrons were initially excited to the conduction band of BiOIO_3 under irradiating UV-light (310 nm) and they in turn relaxed to the oxygen vacancies. Photoluminescence is a surface phenomenon, which is significantly affected by the change of the surface environment [47]. The oxygen vacancies on the surface of the as-prepared BiOIO_3 can form a trapping center and quench the photoluminescence signal [37,48,49]. Fig. 15 showed the PL spectra of the as-prepared photocatalysts by both hydrothermal and calcination methods. The excitation wavelength is 310 nm and all samples possess emission peaks at about 419 nm. Compared to H-150, the intensities of the emission peaks for C-200, C-300 and C-400 samples were substantially lower because of the induced oxygen vacancies. The drastic quenching of the emission clearly indicated that the induced oxygen vacancies could greatly facilitate the separation of the electron-hole pairs [50]. Furthermore, the C-200 emission peak strength is less than that of C-300 and C-400, which may be a main factor that C-200 maintains high photocatalytic performance.

From the above characterizations, we proposed the synthesis mechanism of BiOIO_3 nanomaterials with oxygen vacancies via calcination method. When bismuth nitrate pentahydrate was dispersed in the water, at the beginning, Bi^{3+} cations reacted with H_2O to form $(\text{Bi}_2\text{O}_2)^{2+}$ and H^+ cations, within which the interactions of

Bi and O yield covalent bonds. The pH of the solution was below 7 because of containing numerous H^+ cations. Then the potassium iodate was dissolved in the above solution, providing iodate ion to react with $(\text{Bi}_2\text{O}_2)^{2+}$ in the solution to form numerous small nuclei of BiOIO_3 through the coulomb coupling force. The nuclei of BiOIO_3 were stacked with HNO_3 naturally composed of NO_3^- and H^+ in the solution to form bismuth oxide nitrate hydrate, during which HNO_3 etched the BiOIO_3 samples, inhibiting the development of BiOIO_3 . When being calcined at 200 °C, HNO_3 volatilized and the oxygen vacancies appeared on the surface of the BiOIO_3 samples. Furthermore, with the calcination temperature gradually increasing to 300 °C, the fresh tiny BiOIO_3 slices were stacked together by the Van Der Waals force through the halogen atoms, yielding various building blocks, thus the oxygen vacancies decreased slowly. The synthesis mechanism can be described as the following Eqs. (1–6)



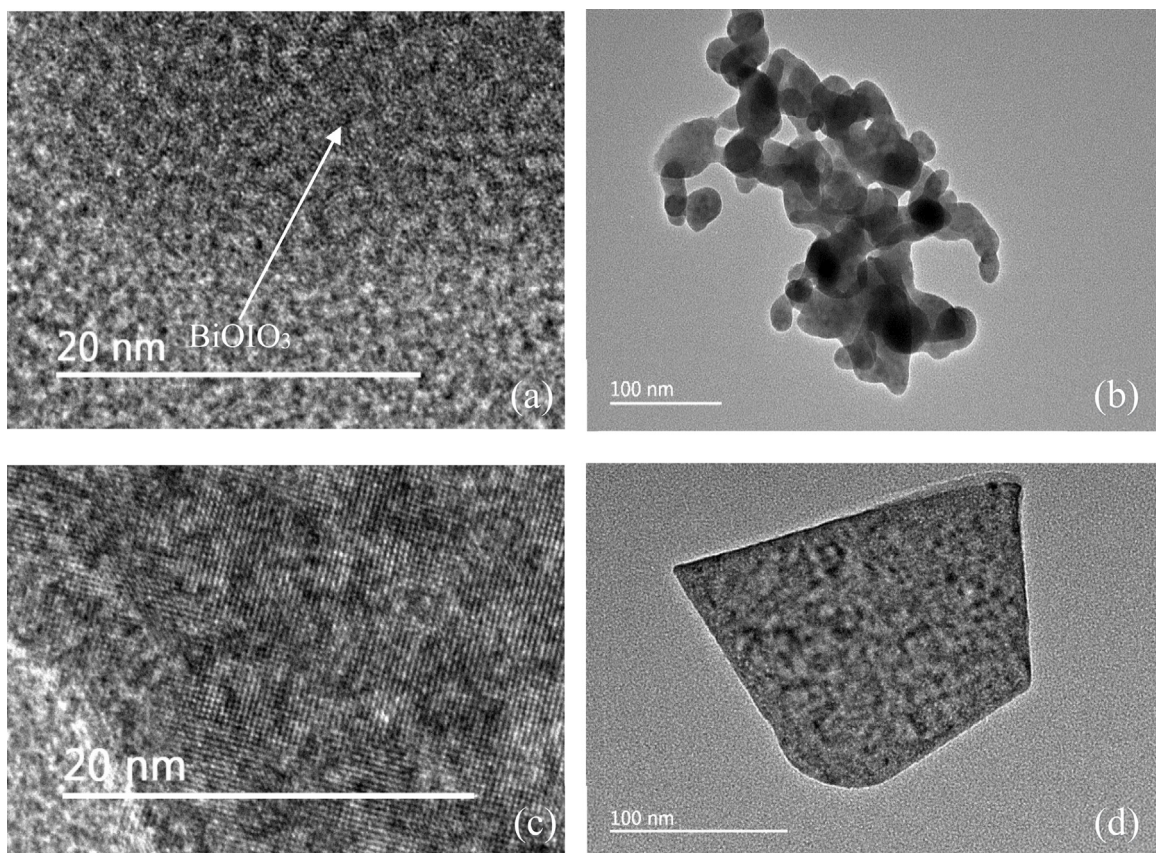


Fig. 10. TEM images of the C-200(a, b) and H-150(c, d).

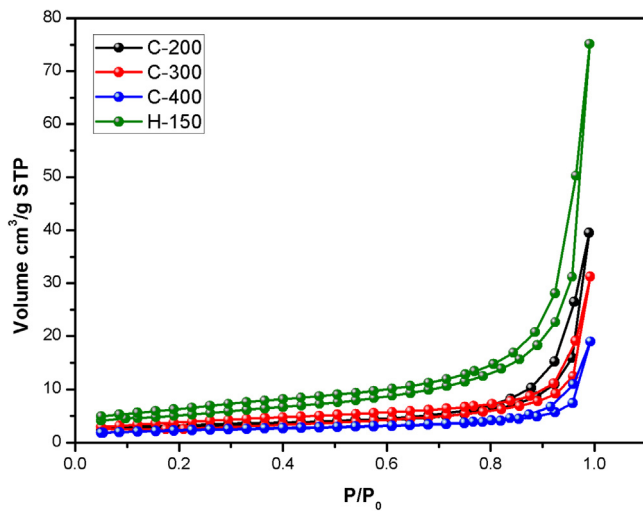


Fig. 11. Nitrogen adsorption-desorption isotherms.

3.2. Photocatalytic properties

3.2.1. Hg⁰ removal under LED irradiation

Hg⁰ removal performance over the BiOIO₃ and Bi₅O₇I nanomaterials fabricated via calcination method and BiOIO₃ nanomaterial fabricated by hydrothermal method were investigated under LED irradiation respectively. Fig. 16 showed the results of the photocatalytic oxidation efficiency of Hg⁰ under the 18W LED irradiation for 1 h by the C-100, C-200, C-300, C-400, C-500, C-600, C-700 and H-150 nanomaterials. The C-200 possesses a higher Hg⁰ removal efficiency under the 18W LED irradiation, which can reach up to

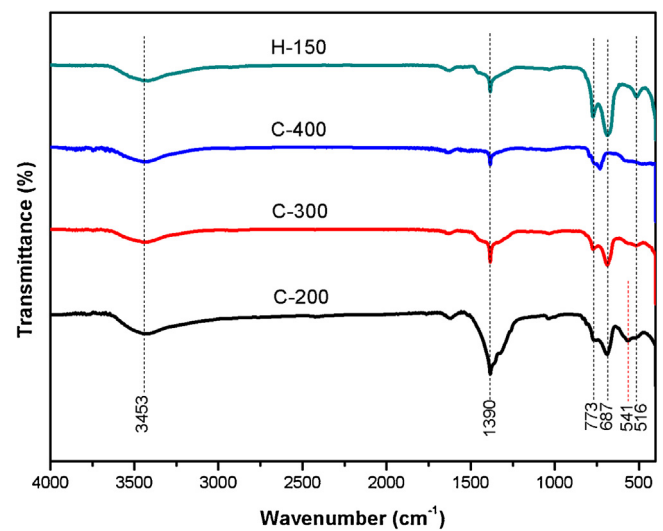


Fig. 12. FT-IR adsorption spectrum of C-200, C-300, C-400, and H-150.

76.3%. The Hg⁰ removal efficiency by C-100 under LED irradiation was 19.1% due to some surface chemisorbed water and nitric acid, which was confirmed by XRD and TGA characterization. The C-300 and C-400 had 67.6% and 58.7% of Hg⁰ removal efficiency under LED irradiation for 1 h respectively. The C-500 and C-600 were Bi₅O₇I photocatalysts, and the Hg⁰ removal efficiency dropped slowly, which means Bi₅O₇I photocatalysts were unstable. The C-500 and C-600 had 33.8% and 35.1% of Hg⁰ removal efficiency after 1 h LED irradiation, indicating that the Bi₅O₇I had a weak Hg⁰ removal performance compared to BiOIO₃ nanomaterial. The C-700 is Bi₂O₃

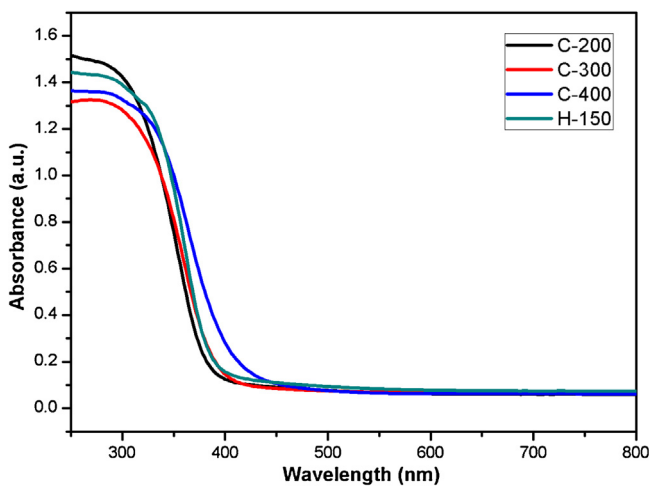


Fig. 13. UV-vis DRS of the C-200, C-300, C-400, and H-150.

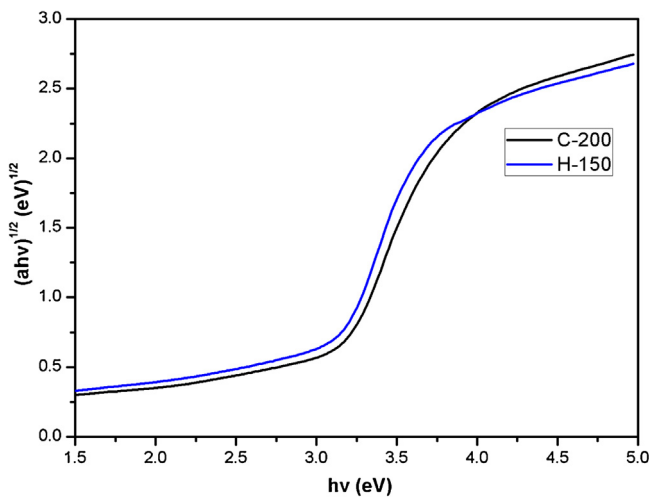


Fig. 14. UV-vis DRS of the C-200, and H-150.

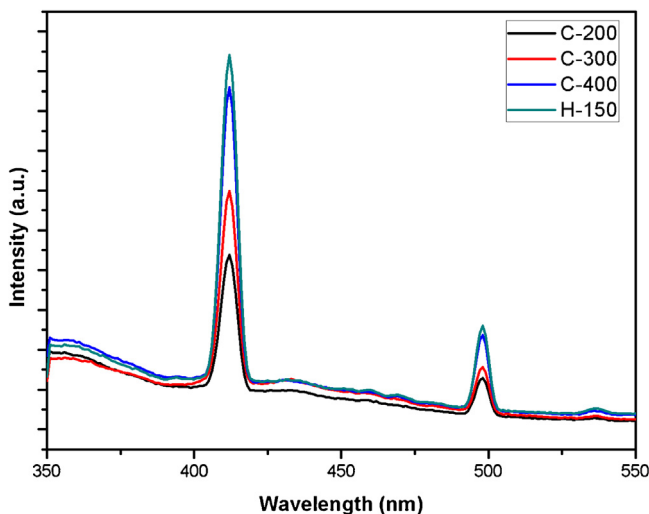


Fig. 15. Photoluminescence spectra of C-200, C-300, C-400, and H-150.

photocatalysts, whose Hg^{00} photocatalytic ability was very weak. The Hg^{00} removal efficiency by H-150 is 57.8%, which is lower than that of the C-200, C-300 and C-400 photocatalysts prepared by calcination method.

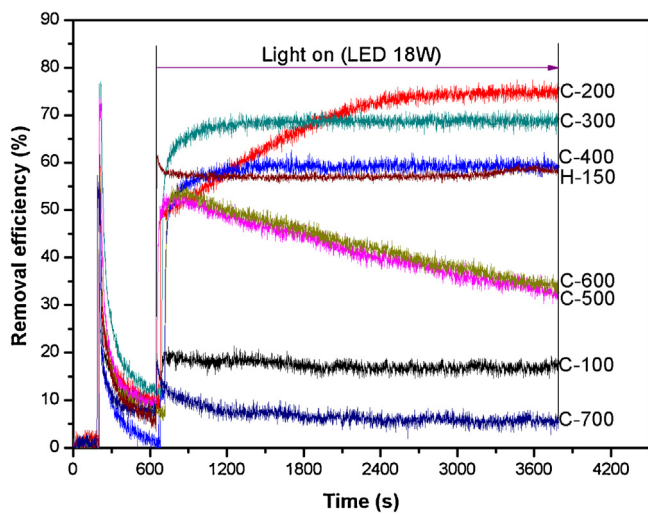


Fig. 16. Hg^{00} photocatalytic oxidation removal efficiency by the C-100, C-200, C-300, C-400, C-500, C-600, C-700 and H-150 under 18W LED irradiation.

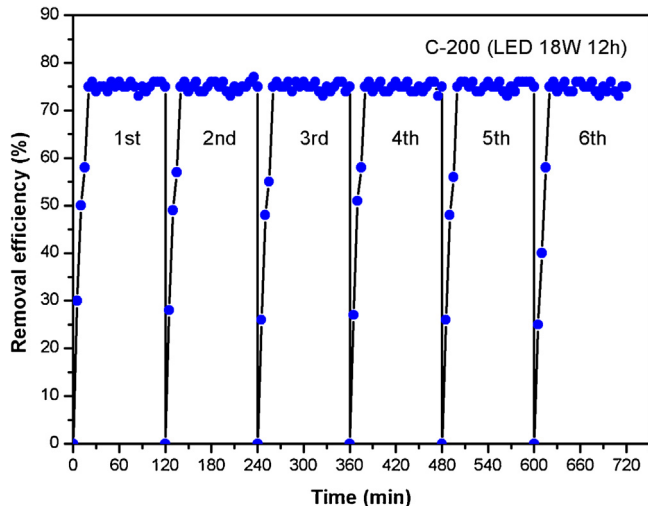


Fig. 17. The stability of C-200 under 18W LED irradiation for 12 h.

3.2.2. Hg^0 removal under LED irradiation for 12 h

The stability of a photocatalyst is very important for its practical application. The C-200 possessed the highest photocatalytic performance, which was up to 76.3% under the testing conditions in consideration, so we chose the C-200 to investigate the stability of photocatalytic performance. Fig. 17 showed the Hg^0 photocatalytic oxidation removal efficiency by C-200 under 18W LED for six circles and each circle underwent for 2 h. As shown in Fig. 17, Hg^0 removal efficiency by C-200 reached up to 76% and the Hg^0 removal efficiency was no change for the total six testing circles, which means that the BiOIO_3 nanomaterials fabricated by calcination method in 200 °C for 2 h have a high stability. Fig. 18 showed the XRD characterization of C-200 nanomaterials before and after 6 testing circles. It can be seen that the crystal texture of the C-200 nanomaterials was no change, confirming the stability of the C-200 nanomaterials.

3.3. Photocatalytic reaction mechanisms

The heterolayered BiOIO_3 photocatalysts containing Bi^{3+} and I^{5-} cations, which are located at the BiO_6 hexagonal and IO_3 trigonal pyramidal sites respectively. The BiO_6 pyramids form the aurivilliustype $(\text{Bi}_2\text{O}_2)^{2+}$ layers, and the polar IO_3^- polyhedra connect

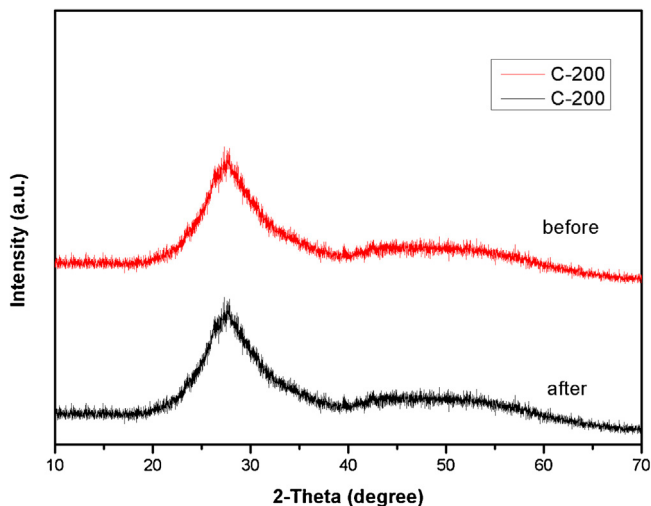


Fig. 18. XRD pattern of the C-200 before and after 12 h test.

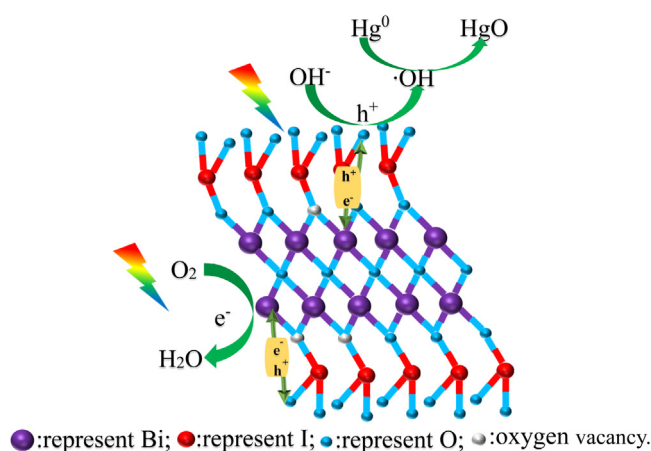


Fig. 19. Mechanism of separation of photo electron-hole pairs.

to a bridging O atom to form a polar iodate. Compared to H-150, the C-200 introduces oxygen vacancies, possessing higher separation efficiency of electron-hole pairs. Shown as Fig. 19, when the light irradiates on photocatalysts, electron-hole pairs are generated from BiOI_3 . The hole goes to the terminal O sites of IO_3^- , meanwhile, the electron goes through the bridging oxygen vacancy and is trapped by Bi^{3+} . The C-200 owns a strong oxidizing ability because the E_g is 3.10 eV. The C-200 has a higher separation efficiency of electron-hole pair, so the hole bonds to OH^- to form $\cdot\text{OH}$. Because the valence band level of C-200, 4.09 eV, became positive with respect to $\cdot\text{OH}/\text{OH}^-$ (+1.99 eV) couple, the $\cdot\text{OH}$ can oxide Hg^0 into HgO . At the same time, the conduction band of C-200 nanomaterials becomes negative with respect to O_2/O_2^- (-0.28 eV) couple, so the electrons bond to O_2 to form H_2O . The photocatalytic oxidation reaction can be described as the following Eqs. (1–5):



4. Conclusions

In summary, we fabricated BiOI_3 photocatalysts via calcination method. Compared to hydrothermal method, calcination method could induce oxygen vacancies for efficient separation of the electron-hole pairs and in turn enhance photocatalytic performance of the as-prepared photocatalysts. HNO_3 naturally yielded in the intermediate product during its preparation etched the resulting BiOI_3 , inhibiting the development of the BiOI_3 . During the calcination process, HNO_3 inside the resulting BiOI_3 volatilized, and the oxygen vacancies appeared on the surface of the BiOI_3 . The C-200, which was prepared with calcination temperature of 200 °C, has a high removal efficiency of Hg^0 , which can reach up to 76% under 18W LED irradiation. In addition, the BiOI_3 photocatalysts fabricated by calcination method possessed a high chemical stability confirmed by six circle tests. This work opens up a new way to fabricate semiconductor photocatalysts containing high concentration of oxygen vacancies, which are benefit for solar energy conversion and pollutant controls.

Acknowledgments

This work was partially sponsored by NSF (Natural Science Foundation, 21237003, 50806041, 51106133, 51606115), Natural Science Foundation of Shanghai (<GN2>16ZR1413500</GN2>), Shanghai Science and Technology Development (15dz1200703, 15110501000) and Science and Technology Support Program of Jiangsu Province(BE2014682).

References

- [1] E.G. Pacyna, J.M. Pacyna, N. Pirrone, European emissions of atmospheric mercury from anthropogenic sources in 1995, *Atmos. Environ.* 35 (2001) 2987–2996.
- [2] E.G. Pacyna, J.M. Pacyna, K. Sundseth, J. Munthe, K. Kindbom, S. Wilson, F. Steenhuizen, P. Maxson, Global emission of mercury to the atmosphere from anthropogenic sources in 2005 and projections to 2020, *Atmos. Environ.* 44 (2010) 2487–2499.
- [3] Emission Standard of Air Pollutants for Power Plants. China, 2011.
- [4] J.H. Pavlish, E.A. Sondreal, M.D. Mann, E.S. Olson, K.C. Galbreath, D.L. Laudal, S.A. Benson, Status review of mercury control options for coal-fired power plants, *Fuel Process. Technol.* 82 (2003) 89–165.
- [5] L. Guasti, C. Simoni, L.T. Mainardi, C. Crespi, M.G. Cimpanelli, G. Gaudio, E. Consolari, S. Cerutti, A. Venco, Global mercury emissions to the atmosphere from anthropogenic and natural sources, *Atmos. Chem. Phys.* 10 (2010) 5951–5964.
- [6] R.K. Srivastava, N. Hutson, B. Martin, F. Princiotta, J. Staudt, Control of mercury emissions from coal-fired electric utility boilers, *Environ. Sci. Technol.* 40 (2006) 1385–1393.
- [7] A.B. Mukherjee, R. Zevenhoven, P. Bhattacharya, K.S. Sajwan, R. Kikuchi, Mercury flow via coal and coal utilization by-products: a global perspective, *Resour. Conserv. Recycl.* 52 (2008) 571–591.
- [8] K. Felsvang, R. Gleiser, G. Juip, K.K. Nielsen, Activated carbon injection in spray dryer/ESP/FF for mercury and toxics control, *Fuel Process. Technol.* 39 (1994) 417–430.
- [9] R. Meij, B.T. Winkel, The emissions and environmental impact of PM 10 and trace elements from a modern coal-fired power plant equipped with ESP and wet FGD, *Fuel Process. Technol.* 85 (2004) 641–656.
- [10] C.L. Senior, A.F. Sarofim, T. Zeng, J.J. Helble, R. Mamani-Paco, Gas-phase transformations of mercury in coal-fired power plants, *Fuel Process. Technol.* 63 (2000) 197–213.
- [11] B. Hall, P. Schager, O. Lindqvist, Chemical reactions of mercury in combustion flue gases, *Water Air Soil Pollut.* 56 (1991) 3–14.
- [12] Y.H. Li, C.W. Lee, B.K. Gullett, The effect of activated carbon surface moisture on low temperature mercury adsorption, *Carbon* 40 (2002) 65–72.
- [13] Y. Yuan, Y. Zhao, H. Li, L. Yang, G. Xiang, C. Zheng, J. Zhang, Electrospun metal oxide-TiO₂ nanofibers for elemental mercury removal from flue gas, *J. Hazard. Mater.* 227–228 (2012) 427.
- [14] Z.K. Zhuang, Z.M. Yang, S.Y. Zhou, H.Q. Wang, C.L. Sun, Z.B. Wu, Synergistic photocatalytic oxidation and adsorption of elemental mercury by carbon modified titanium dioxide nanotubes under visible light LED irradiation, *Chem. Eng. J.* 253 (2014) 16–23.
- [15] H. Shen, I.R. Je, C.S. Yuan, C.H. Hung, The enhancement of photo-oxidation efficiency of elemental mercury by immobilized WO_3/TiO_2 at high temperatures, *Appl. Catal. B Environ.* 195 (2016) 90–103.

- [16] I. Nakamura, N. Negishi, S. Kutsuna, T. Ihara, S. Sugihara, K. Takeuchi, Role of oxygen vacancy in the plasma-treated TiO_2 photocatalyst with visible light activity for NO removal, *J. Mol. Catal. A Chem.* 161 (2000) 205–212.
- [17] J. Wang, P. Liu, X. Fu, Z. Li, W. Han, X. Wang, Relationship between oxygen defects and the photocatalytic property of ZnO nanocrystals in nafion membranes, *Langmuir* 25 (2009) 1218–1223.
- [18] J. Li, Y. Yu, L. Zhang, Bismuth oxyhalide nanomaterials: layered structures meet photocatalysis, *Nanoscale* 6 (2014) 8473–8488.
- [19] H. Zhao, F. Tian, R. Wang, R. Chen, A review on bismuth-related nanomaterials for photocatalysis, *Rev. Adv. Sci. Eng.* 3 (2014) 3–27.
- [20] S.D. Nguyen, J. Yeon, S.H. Kim, P.S. Halasyamani, $\text{BiO}(\text{IO}_3)$: A new polar iodate that exhibits an Aurivillius-type (Bi_2O_2)²⁺ layer and a large SHG response, *ChemInform* 133 (2011) 12422–12425.
- [21] W. Wang, B. Huang, X. Ma, Z. Wang, X. Qin, X. Zhang, Y. Dai, M.H. Whangbo, Efficient separation of photogenerated electron-hole pairs by the combination of a heterolayered structure and internal polar field in pyroelectric BiOIO_3 nanoplates, *Chem. – A Eur. J.* 19 (2013) 14777–14780.
- [22] X.M. Qi, M.L. Gu, X.Y. Zhu, J. Wu, H.M. Long, K. He, Q. Wu, Fabrication of BiOIO_3 nanosheets with remarkable photocatalytic oxidation removal for gaseous elemental mercury, *Chem. Eng. J.* 285 (2016) 11–19.
- [23] X.C. Song, Y.L. Qi, Y.F. Zheng, Enhanced photocatalytic performance of heterojunction $\text{BiOI}/\text{BiOIO}_3$ nanocomposites under simulated solar light, *Nano* (2016).
- [24] H. Huang, K. Xiao, K. Liu, S. Yu, Y. Zhang, In situ composition-Transforming fabrication of $\text{BiOI}/\text{BiOIO}_3$ -Heterostructure: semiconductor p–n junction and dominantly exposed reactive facets, *Crystal Growth Design* 16 (2016) 221–228.
- [25] R. Zhou, J. Wu, J. Zhang, H. Tian, P. Liang, T. Zeng, P. Lu, J. Ren, T. Huang, X. Zhou, Photocatalytic oxidation of gas-phase Hg^0 on the exposed reactive facets of $\text{BiOI}/\text{BiOIO}_3$ heterostructures, *Appl. Catal. B Environ.* (2017) 465–474.
- [26] H. Zhang, C.G. Niu, S.F. Yang, G. Zeng, Facile fabrication of $\text{BiOIO}_3/\text{BiOBr}$ composite with enhanced visible light photocatalytic activity, *RSC Adv.* 6 (2016).
- [27] D.H. Cui, X.C. Song, Y.F. Zheng, A novel $\text{AgI}/\text{BiOIO}_3$ nanohybrid with improved visible-light photocatalytic activity, *RSC Adv.* 6 (2016).
- [28] J. Wu, X. Chen, C. Li, Y. Qi, X. Qi, J. Ren, B. Yuan, B. Ni, R. Zhou, J. Zhang, T. Huang, Hydrothermal synthesis of carbon spheres- $\text{BiOI}/\text{BiOIO}_3$ heterojunctions for photocatalytic removal of gaseous Hg^0 under visible light, *Chem. Eng. J.* 304 (2016) 533–543.
- [29] T. Xiong, F. Dong, Y. Zhou, M. Fu, W.K. Ho, New insights into how RGO influences the photocatalytic performance of $\text{BiOIO}_3/\text{RGO}$ nanocomposites under visible and UV irradiation, *J. Coll. Interf. Sci.* 447 (2015) 16.
- [30] C. Liu, H. Huang, X. Du, T. Zhang, N. Tian, Y. Guo, Y. Zhang, In situ Co-Crystallization for fabrication of $\text{g-C}_3\text{N}_4/\text{Bi}_5\text{O}_7$ heterojunction for enhanced visible-Light photocatalysis, *J. Phys. Chem. C* 119 (2015) 17156–17165.
- [31] Y. Sun, T. Xiong, F. Dong, H. Huang, W. Cen, Interlayer-I-doped BiOIO_3 nanoplates with an optimized electronic structure for efficient visible light photocatalysis, *Chem. Commun.* 52 (2016) 8243.
- [32] X. Pan, M.Q. Yang, X. Fu, N. Zhang, Y.J. Xu, Defective TiO_2 with oxygen vacancies: synthesis, properties and photocatalytic applications, *Nanoscale* 5 (2013) 3601.
- [33] J. Wang, Z. Wang, B. Huang, Y. Ma, Y. Liu, X. Qin, X. Zhang, Y. Dai, Oxygen vacancy induced band-gap narrowing and enhanced visible light photocatalytic activity of ZnO , *ACS Appl. Mater. Interfaces* 4 (2012) 4024.
- [34] W. Yan, C. Feng, Z. Min, J. Yang, Z. Zhang, Enhanced visible light photocatalytic activity of N-doped TiO_2 in relation to single-electron-trapped oxygen vacancy and doped-nitrogen, *Appl. Catal. B Environ.* 100 (2010) 84–90.
- [35] J. Wu, C. Li, X. Zhao, Q. Wu, X. Qi, X. Chen, T. Hu, Y. Cao, Photocatalytic oxidation of gas-phase Hg^0 by CuO/TiO_2 , *Appl. Catal. B Environ.* 176–177 (2015) 559–569.
- [36] A.P. Grosvenor, M.C. Biesinger, R.S.C. Smart, N.S. McIntyre, New interpretations of XPS spectra of nickel metal and oxides, *Surf. Sci.* 600 (2006) 1771–1779.
- [37] Z. Zhang, W. Wang, E. Gao, M. Shang, J. Xu, Enhanced photocatalytic activity of Bi_2WO_6 with oxygen vacancies by zirconium doping, *J. Hazard. Mater.* 196 (2011) 255–262.
- [38] L. Zhang, W. Wang, D. Jiang, E. Gao, S. Sun, Photoreduction of CO_2 on BiOCl nanoplates with the assistance of photoinduced oxygen vacancies, *Nano Res.* 8 (2015) 821–831.
- [39] X.Y. Kong, Y.Y. Choo, S.P. Chai, K.S. Ai, A.R. Mohamed, Oxygen vacancies induced Bi_2WO_6 for realization of full solar spectrum photocatalytic CO_2 reduction: from UV to NIR region, *Chem. Commun.* (2016).
- [40] C. Zheng, G. He, X. Xiao, M. Lu, H. Zhong, X. Zuo, J. Nan, Selective photocatalytic oxidation of benzyl alcohol into benzaldehyde with high selectivity and conversion ratio over $\text{Bi}_4\text{O}_5\text{Br}_2$ nanoflakes under blue LED irradiation, *Appl. Catal. B Environ.* (2016).
- [41] Y. Huang, H. Li, M.S. Balogun, W. Liu, Y. Tong, X. Lu, H. Ji, Oxygen vacancy induced bismuth oxyiodide with remarkably increased visible-light absorption and superior photocatalytic performance, *ACS Appl. Mater. Interfaces* 6 (2014) 22920–22927.
- [42] Y. Guo, J. Li, Z. Gao, X. Zhu, Y. Liu, Z. Wei, W. Zhao, C. Sun, A simple and effective method for fabricating novel p–n heterojunction photocatalyst $\text{g-C}_3\text{N}_4/\text{Bi}_4\text{Ti}_3\text{O}_12$ and its photocatalytic performances, *Appl. Catal. B Environ.* 192 (2016) 57–71.
- [43] Y. Lv, W. Yao, R. Zong, Y. Zhu, Fabrication of wide-range-visible photocatalyst $\text{Bi}_2\text{WO}_{6-x}$ nanoplates via surface oxygen vacancies, *Sci. Rep.* 6 (2015) 19347.
- [44] H. Ma, M. Zhao, H. Xing, Y. Fu, X. Zhang, X. Dong, Synthesis and enhanced photoreactivity of metallic Bi-decorated BiOBr composites with abundant oxygen vacancies, *J. Mater. Sci.: Mater. Electron.* 26 (2015) 10002–10011.
- [45] M. Yoshikawa, H. Seki, K. Inoue, K. Matsuda, Y. Tanahashi, H. Sako, Y. Nanen, M. Kato, T. Kimoto, Characterization of silicon dioxide films on a 4H-SiC Si(001) face by fourier transform infrared (FT-IR) spectroscopy and cathodoluminescence spectroscopy, *Appl. Spectrosc.* 65 (2011) 543–548.
- [46] Y. Qi, L. Pan, L. Ma, P. Liao, J. Ge, D. Zhang, Q. Zheng, B. Yu, Y. Tang, D. Sun, Investigation on FT-IR spectra and dielectric property of PVDF/inorganic composites, *J. Mater. Sci.: Mater. Electron.* 24 (2013) 1446–1450.
- [47] B. Santara, P.K. Giri, K. Imakita, M. Fujii, Evidence of oxygen vacancy induced room temperature ferromagnetism in solvothermally synthesized undoped TiO_2 nanoribbons, *Nanoscale* 5 (2013) 5476.
- [48] L. Jing, Y. Qu, B. Wang, S. Li, B. Jiang, L. Yang, W. Fu, H. Fu, J. Sun, Review of photoluminescence performance of nano-sized semiconductor materials and its relationships with photocatalytic activity, *Solar Energy Mater. Solar Cells* 90 (2006) 1773–1787.
- [49] K. Lai, W. Wei, Y. Zhu, M. Guo, Y. Dai, B. Huang, Effects of oxygen vacancy and N-doping on the electronic and photocatalytic properties of Bi_2MO_6 ($\text{M}=\text{Mo}, \text{W}$), *J. Solid State Chem.* 187 (2012) 103–108.
- [50] J. Ding, Z. Dai, F. Qin, H. Zhao, S. Zhao, R. Chen, Z-scheme $\text{BiO}_{1-x}\text{Br}/\text{Bi}_2\text{O}_2\text{CO}_3$ photocatalyst with rich oxygen vacancy as electron mediator for highly efficient degradation of antibiotics, *Appl. Catal. B Environ.* (2016).